TOPICAL REVIEW • OPEN ACCESS

Photonic-crystal lasers with high-quality narrow-divergence symmetric beams and their application to LiDAR

To cite this article: Masahiro Yoshida *et al* 2021 *J. Phys. Photonics* **3** 022006

View the article online for updates and enhancements.

Journal of Physics: Photonics

TOPICAL REVIEW

Photonic-crystal lasers with high-quality narrow-divergence symmetric beams and their application to LiDAR

Masahiro Yoshida[1,*] ⓘ, Menaka De Zoysa[2,*] ⓘ, Kenji Ishizaki[1,*] ⓘ, Wataru Kunishi[1,3], Takuya Inoue[2] ⓘ, Koki Izumi[1], Ranko Hatsuda[1] and Susumu Noda[1,2] ⓘ

[1] Department of Electronic Science and Engineering, Kyoto University, Kyoto 615-8510, Japan
[2] Photonics and Electronics Science and Engineering Center, Kyoto University, Kyoto 615-8510, Japan
[3] Research and Development Center, ROHM Co., Ltd., Kyoto 615-8585, Japan
* These authors contributed equally to this work.

E-mail: snoda@kuee.kyoto-u.ac.jp

Abstract

Light detection and ranging (LiDAR) is a key technology for smart mobility of robots, agricultural and construction machines, and autonomous vehicles. However, current LiDAR systems often rely on semiconductor lasers with low-quality, large-divergence, and asymmetric beams, requiring high-precision integration of complicated lens systems to reshape the beam. Also, due to the broad linewidth and the large temperature dependence of their lasing spectrum, a bandpass filter with broad bandwidth must be used in front of the detector, so the detected signal is affected by noise from background light such as sunlight. These critical issues limit the performance, compactness, affordability, and reliability of the LiDAR systems. Photonic-crystal surface-emitting lasers (PCSELs) have attracted much attention as novel semiconductor lasers that can solve the issues of conventional semiconductor lasers owing to their capability of high-quality, very-narrow-divergence, and symmetric beam operation supported by broad-area band-edge resonance in their two-dimensional photonic crystal. In this paper, we show the progress and the state of the art of broad-area coherent PCSELs and their application to a time-of-flight (ToF) LiDAR system. We first review the progress of PCSELs made so far. Next, we show recent progress based on PCSELs with a double-lattice structure that enables higher-power and narrower-divergence operation while keeping a symmetric beam shape. By optimizing the double-lattice photonic crystal and the reflective properties of a backside distributed Bragg reflector (DBR), we achieve a high peak power of 10 W while maintaining a nearly diffraction-limited beam divergence of $\sim 0.1°$ (FWHM) from a 500 μm diameter resonator. Using this PCSEL, we construct a LiDAR system that uses no external lens system in its light source and demonstrate highly spatially resolved ToF sensing (measurement range of ~ 20 m), which is appropriate for autonomous robots and factory automation.
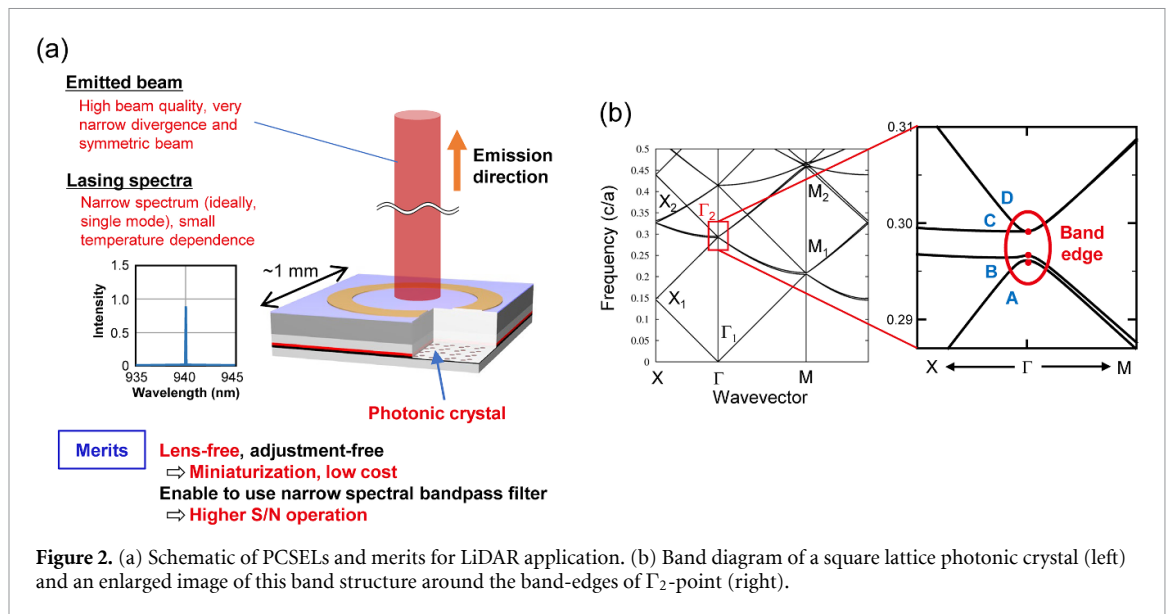
1. Introduction

Light detection and ranging (LiDAR) is one of the most important sensing technologies for smart mobility of robots, agricultural and construction machines, and autonomous vehicles [1–3]. Figure 1(a) shows a schematic illustration of a typical LiDAR system using a time-of-flight (ToF) method. An optical pulse emitted from a laser source is scanned by a beam-scanning device (e.g. a rotating mirror [4]) and irradiated on a measured object. A part of the light reflected and scattered at the object is detected by a photodetector. A bandpass filter is placed in front of the detector to filter out background light such as sunlight, leading to a reduction of detection noise. One can measure the distance between the LiDAR system and the object based on the time difference between the emission of the optical pulse and the detection of the reflected light. For practical, high-performance LiDAR systems, the light source is of critical importance. For ToF LiDAR, a
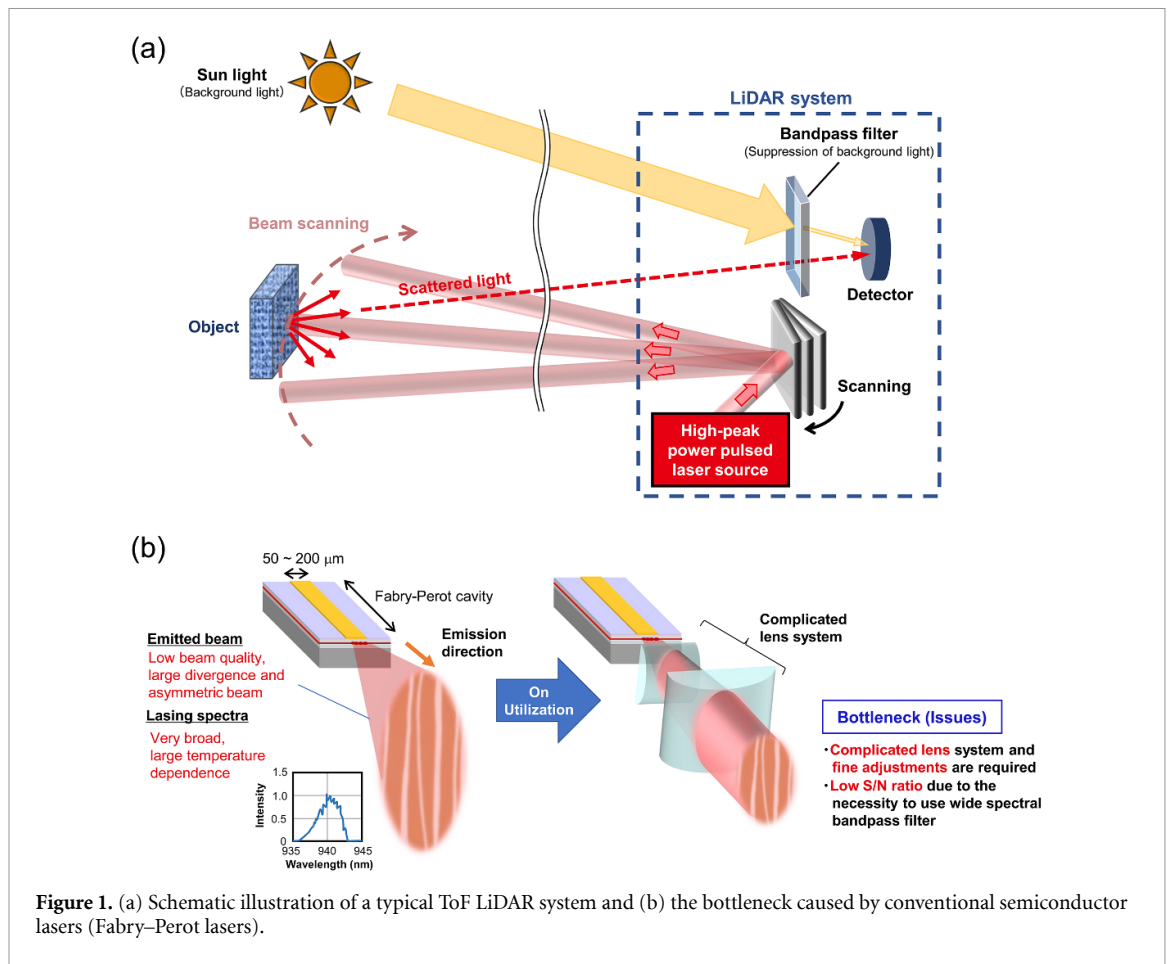
Figure 1. (a) Schematic illustration of a typical ToF LiDAR system and (b) the bottleneck caused by conventional semiconductor lasers (Fabry–Perot lasers).

pulse laser source with a high peak power and a narrow beam divergence is required for long-distance, high-spatial-resolution ranging. To improve the signal-to-noise (S/N) ratio using a narrow bandpass filter, it is also desirable that the laser source has a narrow spectral linewidth and a small temperature dependence. However, existing ToF LiDAR systems mostly rely on conventional, Fabry–Perot-type (FP) semiconductor lasers as the light source, which struggle to meet the above requirements due to their undesirable features inherent to their edge-emitting resonators as shown in figure 1(b). Specifically, FP-lasers have large, asymmetric beam-divergence angles of >30° along their fast axis and >10° along their slow axis. Also, these lasers exhibit unavoidable multi-mode oscillation caused by expansion of their emission area, which degrades their beam quality. Furthermore, single FP emitters suffer from insufficient output power, requiring multiple emitters, which operate incoherently, to be stacked in an array configuration. Out of necessity borne from these issues, the existing ToF LiDAR systems must rely on careful beam reshaping using a complicated series of lenses in an attempt to obtain a beam with the requisite high peak power and narrow divergence. In addition, due to the broad linewidth and large temperature dependence of the lasing spectrum of FP-lasers, a bandpass filter with a broad bandwidth must be used in front of the detector, so the detected signal is affected by noise from the background. Altogether, these systems suffer from issues of performance, size, cost, and reliability. If semiconductor lasers with broad-area coherent resonance could be realized, then a high-power and symmetric, narrow-divergence beam with a narrow spectral width could be obtained from a single laser chip without the use of any external lens, enabling the development of next-generation LiDAR systems that are much smaller, simpler, and functional than the existing ones. The use of lens-free lasers in these next-generation systems would also obviate the need for optical alignment, simplifying the assembly process.

Photonic-crystal surface-emitting lasers (PCSELs) (figure 2(a)) have attracted much attention as novel semiconductor lasers that can solve the above issues of conventional semiconductor lasers [5–16]. PCSELs use the effect of band-edge resonance of a two-dimensional (2D) photonic crystal for lasing. A typical band diagram in a square-lattice photonic crystal is shown in figure 2(b) as an example, where the band edge lying at the Γ_2-point is typically utilized for lasing oscillation, in which various light waves, including four fundamental Bloch waves propagating in the Γ-X directions and also higher-order Broch waves, are coupled with each other to form a 2D standing wave, or 2D coherent resonance [15]. Owing to their capability of preserving such 2D coherent resonance over very broad areas, PCSELs have the potential for high-power and

Figure 2. (a) Schematic of PCSELs and merits for LiDAR application. (b) Band diagram of a square lattice photonic crystal (left) and an enlarged image of this band structure around the band-edges of Γ_2-point (right).

high-beam-quality operation. In particular, the surface-emitted beam has a symmetric circular shape and a very narrow divergence angle proportional to the coherent lasing area, and thus no external lenses are needed for beam reshaping and collimation. In addition, the narrow linewidth and small temperature dependence ($\leqslant 1/3$ of that of FP-lasers) of the lasing spectrum, which is fixed by the lattice constant of the photonic crystal, allow the use of a narrow bandpass filter to filter out background light in front of the detector of the LiDAR system, leading to a higher S/N operation. These unique features are desirable for LiDAR applications.

In the following, we first review the progress of PCSELs made so far. Next, we show recent progress for improvement of device performance based on a double-lattice structure that enables higher-power and narrower-divergence operation while keeping a symmetric beam shape. By optimizing the double-lattice photonic crystal and the reflective properties of a backside distributed Bragg reflector (DBR) mirror, we achieve a high peak power of 10 W while maintaining a nearly diffraction-limited beam divergence of ∼0.1° (FWHM) from a 500 μm diameter resonator. Using this PCSEL, we construct a LiDAR system that uses no external lens system in its light source and demonstrate highly spatially resolved ToF sensing, which is appropriate for autonomous robots and factory automation.

2. Brief review of the progress in PCSELs

Figure 3 summarizes the progress in PCSEL technology. In 1999, 2D coherent lasing oscillation was proposed and demonstrated [5] in semiconductor gain materials using a band-edge mode at the Γ-point of a triangular-lattice photonic crystal, where the output beam was coupled out in the surface-normal direction, enabling surface-emitting operation [5, 8]. Note that separately and almost simultaneously, the use of a band-edge mode at the *X*- (or *M*-)point of a triangular-lattice photonic crystal for lasing oscillation in organic gain material was also reported [17]. However, the latter report did not show coherent 2D resonance, because the light waves propagating in different directions cannot couple two-dimensionally into each other at the band-edges of the *X*- (or *M*-)point of the triangular-lattice structure. On the other hand, at the band-edges of the Γ-point reported in [5, 8], the light waves can couple both one- and two-dimensionally, leading to truly coherent 2D resonance.

Although the first demonstration and early research on PCSELs were performed by using a triangular-lattice photonic crystal, the focus of later research shifted to lasing oscillation at the Γ-point of a square-lattice photonic crystal (as already described in figure 2(b)), which is more suitable for high-power single-mode operation of PCSELs [10, 14, 16] with controllable polarization and beam shape [7, 10, 18, 19] (see the second panel from the left in figure 3). To achieve stable 2D coherent oscillation of PCSELs with square-lattice photonic crystal structures, it is especially important to form photonic crystals with a large refractive index contrast, for example, by embedding air holes (or voids) into the semiconductor material. This is because the four fundamental Bloch waves which oscillate in a mode with transverse-electric (TE) polarization (a typical polarization used for lasing oscillation in the semiconductor gain material) in the square-lattice photonic crystal cannot be coupled directly, and instead are coupled indirectly through the
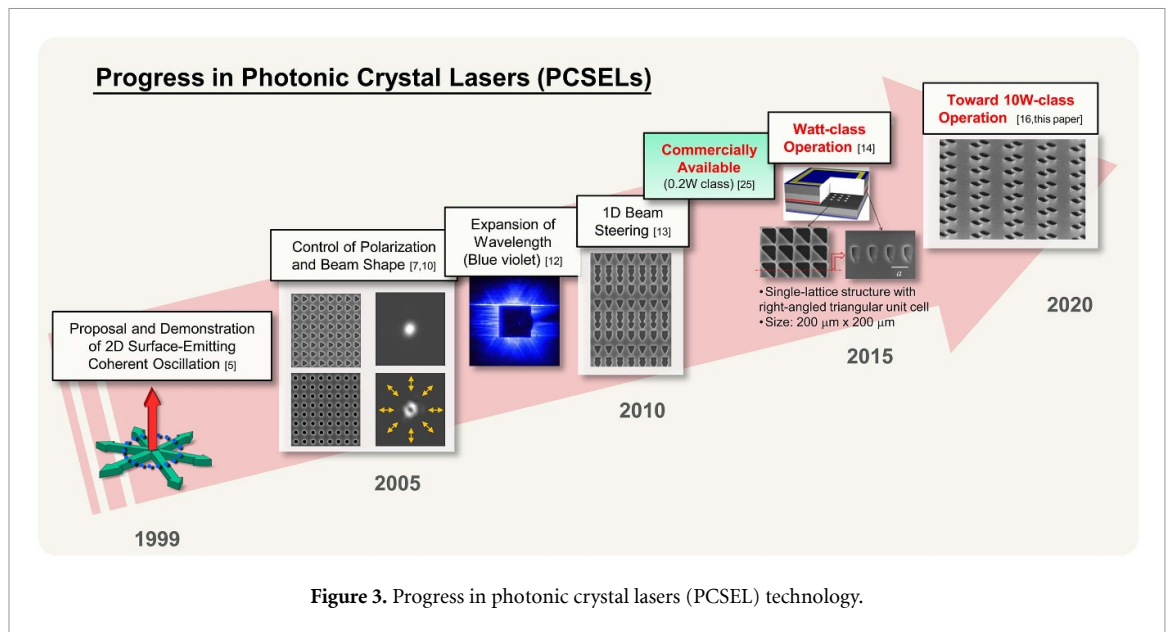
**Figure 3.** Progress in photonic crystal lasers (PCSEL) technology.

higher-order Bloch waves [15, 16, 20–22]. Such indirect coupling through the higher-order waves can be achieved only by introducing a large refractive index contrast.

Following the initial demonstration of the PCSEL and the realization of controllable polarization and beam shape, the lasing wavelength was extended to the visible (blue-violet) regime [12], and unique one-dimensional (1D) beam-steering functionality [13] (see the third and fourth panels from the left in figure 3) was realized. In the early stages of PCSEL development, a wafer-bonding method was initially used to embed the air holes inside the device. Later on, this method was replaced by an advanced air-hole-retained epitaxial regrowth method based on metal-organic vapor phase epitaxy (MOVPE), which is more suitable for high-power and high-beam-quality operation of the PCSELs [14, 16, 23, 24]. In 2014, PCSELs with a 200 μm $\times$ 200 μm device area, whose photonic crystal had a single lattice of right-angle-triangular air holes, were developed by the MOVPE regrowth method, and watt-class, high-power, high-beam-quality operation was successfully demonstrated [14]. A 0.2 W class device based on these photonic crystals has been commercially available since 2013 [25]. In recent years, trials to realize 10 W class operation have been conducted; the results of these trials are described in the next section.

3. 10 W high-power narrow-beam-divergence operation of PCSELs

3.1. Concept of double-lattice photonic crystals

To realize 10 W class high-power, narrow-beam-divergence operation, lasing oscillation in the fundamental mode should be maintained, and oscillation in high-order modes should be suppressed, as the lasing area is expanded. However, the threshold gain margin, defined as the threshold gain difference ($\Delta\alpha$) between the fundamental lasing mode and 1st high-order mode, shrinks as the lasing area increases, leading to the commencement of oscillation in the high-order mode. To overcome this challenge, we have proposed a unique double-lattice structure [16, 26], where two lattices, A and B, are combined as shown in figure 4(a). In this double-lattice structure, the optical path difference between the light diffracted backward by individual lattices is set to be around $\lambda/2$ (where λ is the wavelength in the material), which leads to the destructive interaction of waves diffracted in-plane by 180°. As a result of this interaction, optical modes formed in the double-lattice photonic crystal spread out and leak more easily from the edges of the lasing area than from those edges of the previous single-lattice photonic crystal [14], as shown in figure 4(b). In particular, since the antinodes of the high-order modes are concentrated near the edges, their edge loss (i.e. in-plane loss) increases more quickly than that of the fundamental mode, and the threshold gain margin widens as a consequence. Figure 4(c) shows the calculated results of $\Delta\alpha$ for a double-lattice photonic crystal designed for 500 μmΦ resonators and referred to as structure II in [16]. Using $\Delta\alpha$ of a single-lattice photonic crystal as a benchmark ($\Delta\alpha \sim 4$ cm^{-1} at 200 μmΦ) [14], the resonator area can be increased to 500 μmΦ while maintaining high-beam-quality operation. In this design, we have separately introduced a difference in the heights of the double-hole pair in order to create vertical asymmetry (see the right panel of figure 4(c)), which enhances the surface emission. In other words, the vertical asymmetry is introduced to obtain a reasonable value of radiation constant α_v.
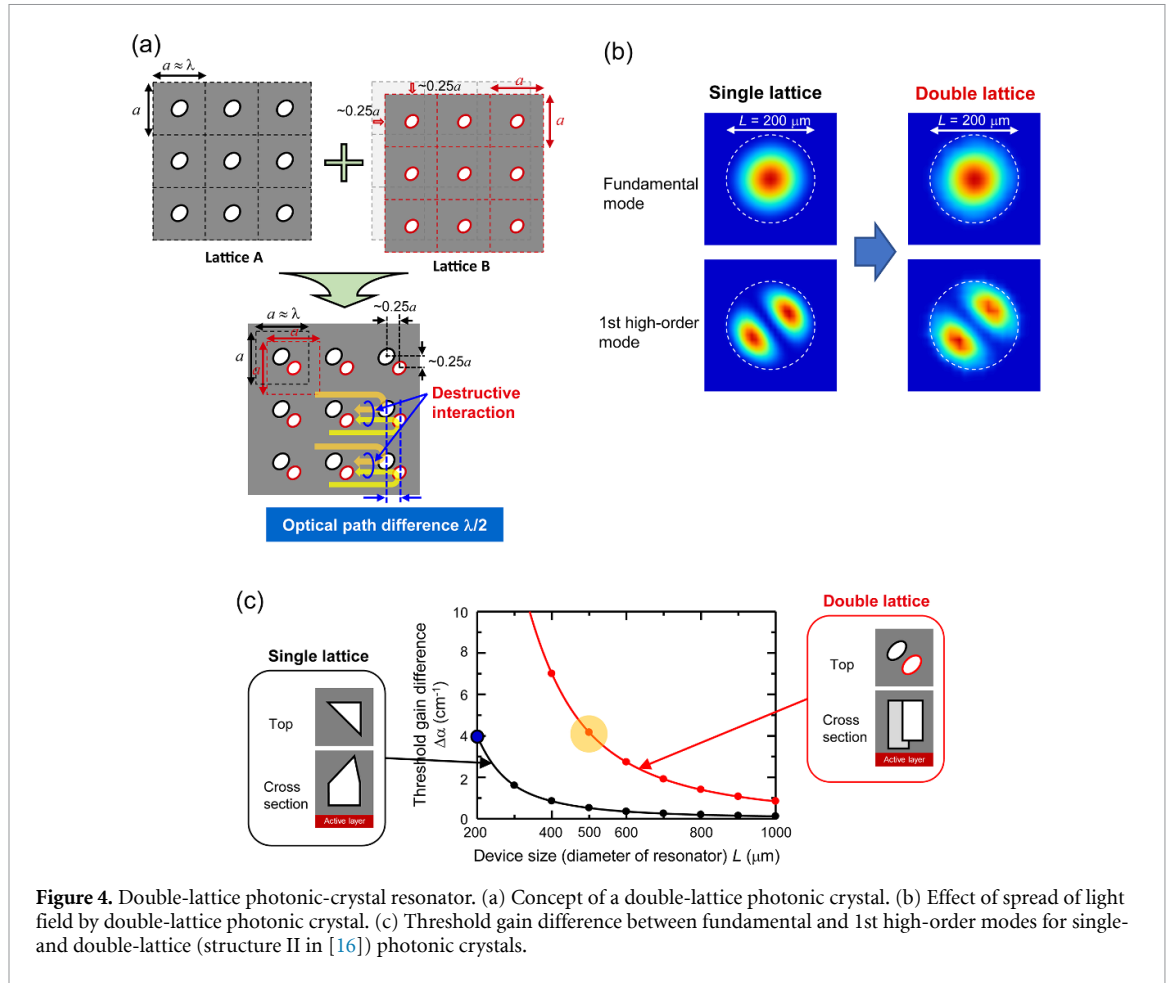
Figure 4. Double-lattice photonic-crystal resonator. (a) Concept of a double-lattice photonic crystal. (b) Effect of spread of light field by double-lattice photonic crystal. (c) Threshold gain difference between fundamental and 1st high-order modes for single- and double-lattice (structure II in [16]) photonic crystals.

We fabricated PCSELs using the double-lattice design, and achieved 10 W high-power, high-beam-quality (beam-divergence angle of ∼0.2° measured at FWHM) operation under pulsed conditions [16]. However, the slope efficiency of this device was ∼0.4 W A^{-1}, and thus a high injection current was necessary to obtain the high output power of 10 W. Also, concerning device fabrication, a relatively complicated process (two-step electron-beam (EB) lithography and dry etching, including careful alignment) was required for forming air-hole pairs with the same shape but different heights, as necessary to obtain the reasonable value of α_{v} [16]. In the following sections, for the purpose of solving all of the above issues inherent to the previous design of double-lattice photonic crystal, we present and discuss optimization of the photonic-crystal design, as well as the use of backside refection by a DBR mirror.

3.2. Optimization of double-lattice photonic crystal for 500 μmΦ PCSEL

We begin by designing a photonic-crystal structure that can be fabricated by a simplified process using one-step EB lithography and etching for 500 μmΦ PCSELs while maintaining a sufficiently wide threshold gain margin for oscillation in the fundamental mode. We investigate an asymmetric structure consisting of two holes with different in-plane shapes in lieu of a height difference in order to enhance the surface-emitted power while maintaining $\Delta\alpha$. Specifically, as shown in figure 5(a), asymmetry is introduced by making one hole elliptical by changing the ratio of its minor (x) and major (y) axes while keeping the other hole circular. Here, the ratio is tuned by fixing x and changing y.
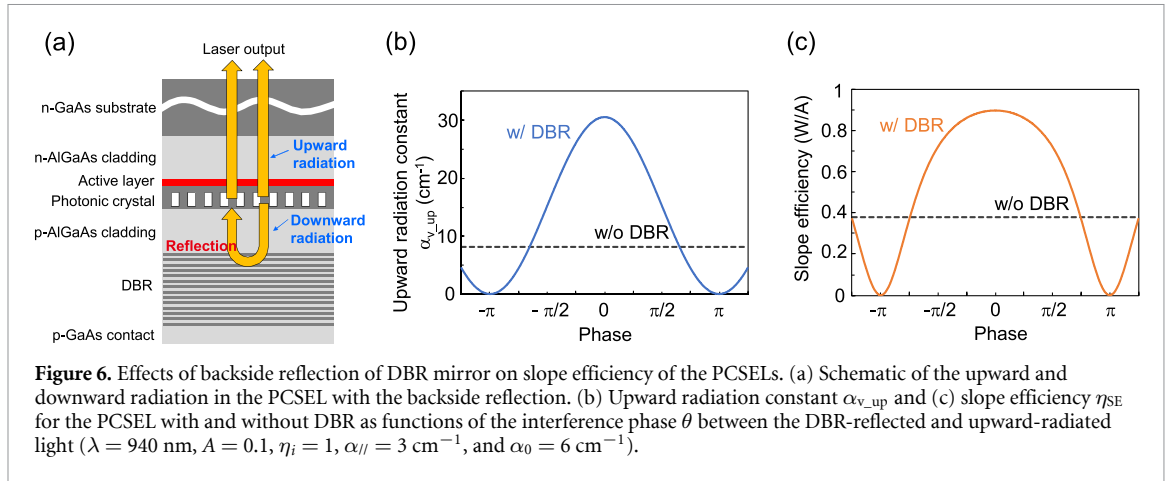
First, we calculate the radiation constant α_{v} of the band-edge mode A in which the lasing oscillation occurs, as a function of the x/y ratio; the dark blue line in figure 5(b) indicates these values of α_{v} when the lattice separation is $d = 0.250a$. α_{v} is 0 when the two holes are circular ($x/y = 1.0$), but increases when the hole becomes elliptical, and is maximum at $x/y = 0.7$. This trend is explained by changes in the cancellation of the electric fields emitted in the surface-normal direction, depending on the degree of electric-field overlap at each hole. Note that the cancellation discussed here does not involve Bloch waves diffracted in-plane and the determination of $\Delta\alpha$, but rather involves the light emitted in the surface-normal direction and the determination of α_{v}. Figure 5(c) shows the calculated electric-field distribution of the mode of band-edge A in the unit cell for $x/y = 1.0$, 0.7, and 0.5. When unit cell has $C_{2\mathrm{v}}$ symmetry ($x/y = 1.0$), the
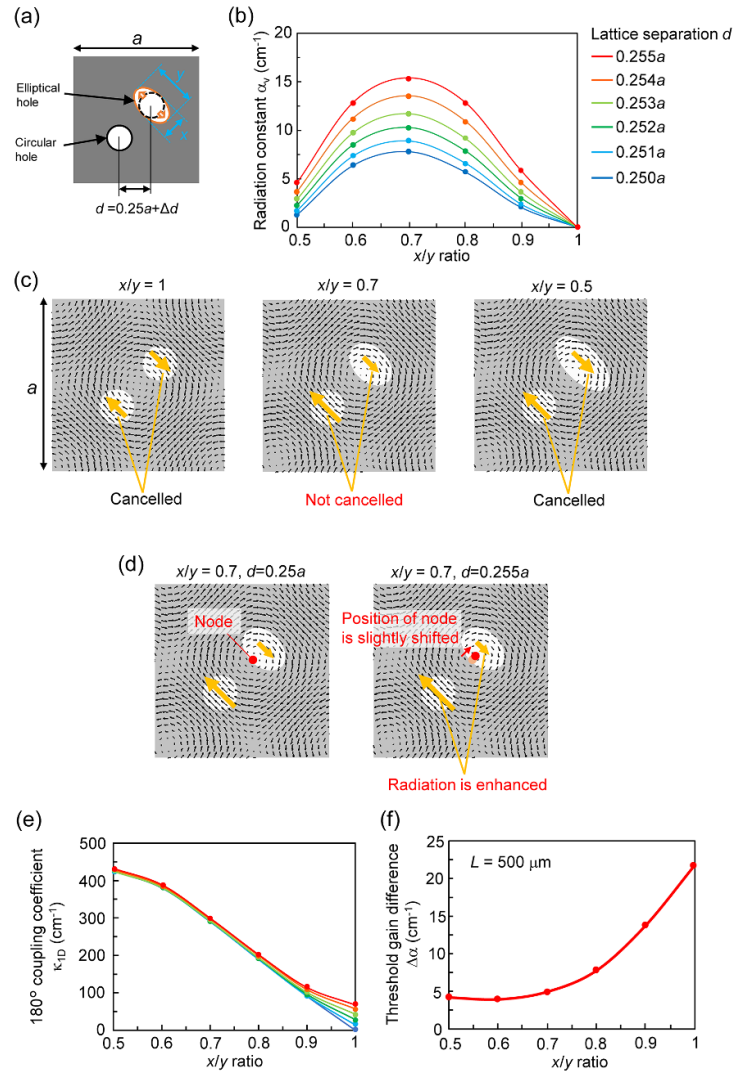
Figure 5. Design of photonic crystal structure for 500 μmΦ PCSEL that can be made by one-step EB lithography and dry etching. (a) Schematic of air hole shape in the unit cell. (b) Radiation constant of band-edge A for various x/y ratio and lattice separation. (c), (d) Electric field distribution in the unit cell. (e) In-plane 180° coupling coefficient for various x/y ratio and lattice separation. (f) Threshold gain difference for various x/y ratio ($d = 0.255a$).

position of the node of the electric field is equidistant from the center of each hole. Consequently, the vectors of the electric fields diffracted out-of-plane at the two holes are equal in magnitude and opposite in phase, resulting in their complete cancellation and thus zero-valued α_v. On the other hand, when C_{2v} symmetry is broken by making one hole elliptical, such cancellation becomes incomplete. In the case of $x/y = 0.7$, the position of the node of the electric field shifts toward the elliptical hole and that of the antinode shifts toward the circular hole, resulting in an imbalance of the magnitude of the vertically diffracted electric-field vectors and thus alleviating their cancellation. However, when the hole becomes even more elliptical ($x/y = 0.5$), the overlap between the elliptical hole and the electric field increases, so the magnitude of its corresponding vertically diffracted electric-field vector approaches that of the circular hole. Therefore, the cancellation once again becomes more complete and α_v decreases. Here, although we have increased α_v by appropriately breaking C_{2v} symmetry as described above, α_v nevertheless does not exceed 7 cm^{-1} even at its maximum at $x/y = 0.7$; considering the presence of other losses in the current device system (e.g. fundamental absorptive loss α_0 and in-plane loss $\alpha_{//}$, which will be discussed later), this value is slightly insufficient. Note that when α_0 is decreased in the future by optimizing the device structure even further, then even a small α_v will be sufficient. To further increase α_v, we consider the lattice separation d between the two holes as an additional degree of freedom for finely tuning the degree of overlap between the holes and the electric field. As shown in figure 5(b), α_v increases as d increases from 0.250a to 0.255a. When d increases, the position of the electric-field node slightly shifts as if it is pulled by the larger elliptical hole, and the imbalance of the diffracted electric-field vectors is enhanced (see figure 5(d)). As a result, a larger radiation coefficient of $\sim$16 cm^{-1} is obtained when $d = 0.255a$ and $x/y = 0.7$; this value is sufficient for obtaining a high slope

Figure 6. Effects of backside reflection of DBR mirror on slope efficiency of the PCSELs. (a) Schematic of the upward and downward radiation in the PCSEL with the backside reflection. (b) Upward radiation constant $\alpha_{\text{v\_up}}$ and (c) slope efficiency η_{SE} for the PCSEL with and without DBR as functions of the interference phase θ between the DBR-reflected and upward-radiated light ($\lambda = 940$ nm, $A = 0.1$, $\eta_i = 1$, $\alpha_{//} = 3$ cm^{-1}, and $\alpha_0 = 6$ cm^{-1}).

efficiency exceeding $\sim$0.8 W A^{-1} once the effect of reflection from a DBR is considered as well, as discussed later.

Next, we evaluate whether the above design for realizing appropriate α_{v} is also appropriate for achieving a reasonably large value of threshold gain difference $\Delta\alpha$ to realize high-beam-quality operation in a 500 μmΦ device. Figure 5(e) shows κ_{1D}, a coupling coefficient which expresses the strength of in-plane 180° diffraction, as a function of the x/y ratio for structures with different d. It is seen that κ_{1D} increases as the x/y ratio decreases from 1.0 to 0.5. Nevertheless, a sufficiently small value of κ_{1D} of less than 300 cm^{-1}, which is comparable to that of our previous design, is obtained at around $x/y = 0.7$. Figure 5(f) shows the calculated $\Delta\alpha$ as a function of the x/y ratio for a structure with $d = 0.255a$ in a 500 μmΦ device. As shown in this figure, although $\Delta\alpha$ decreases as the x/y ratio decreases (or, alternatively, as κ_{1D} increases), a sufficiently large $\Delta\alpha$ of $\sim$5 cm^{-1} is nevertheless obtained when $x/y = 0.7$. Therefore, a coincidence of high-peak-power and high-beam-quality operation is expected from a 500 μmΦ device using this new photonic crystal structure which can be fabricated using a simplified process.

3.3. Effects of backside reflection of DBR mirror

Next, we discuss improving the slope efficiency of the PCSEL by introducing and optimizing a DBR mirror on the backside of the device to act as a reflector. The slope efficiency η_{SE} of a PCSEL without the DBR mirror is expressed by the following equation:

$$\eta_{\text{SE}} = \frac{1.24}{\lambda}(1 - A)\eta_i \frac{\alpha_{\text{v\_up}}}{\alpha_{\text{v\_up}} + \alpha_{\text{v\_down}} + \alpha_{\parallel} + \alpha_0} \tag{1}$$
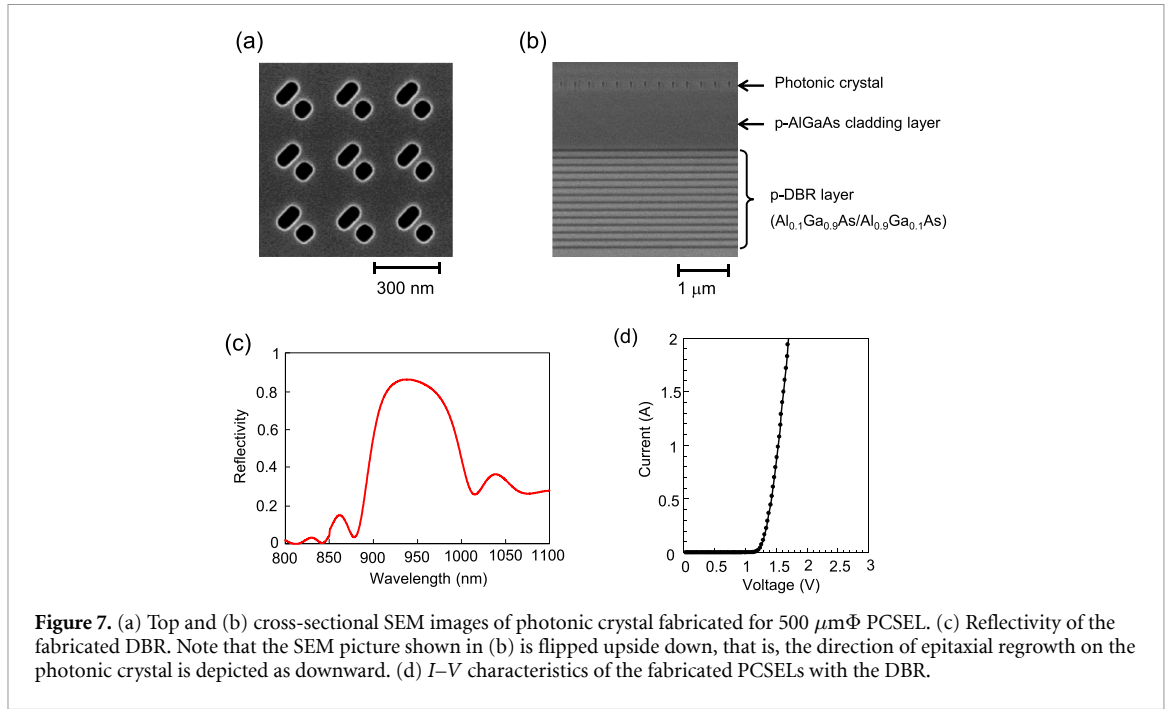
where $\alpha_{\text{v\_up}}$ and $\alpha_{\text{v\_down}}$ are the upward and downward radiation constants and their sum is equal to the α_{v} discussed above, α_0 is the fundamental absorptive loss, $\alpha_{//}$ is the in-plane loss, and λ is the lasing wavelength. A is an absorption constant, which is defined as the ratio of the power absorbed in the substrate to the total output power from the resonator, and η_i is the internal quantum efficiency of the active layer. Because nearly equal amounts of light are diffracted from the photonic crystal layer in the upward and downward directions (i.e. $\alpha_{\text{v\_up}} \approx \alpha_{\text{v\_down}} \approx \alpha_{\text{v}}/2$), the introduction of the DBR mirror, which reflects the downward-diffracted light toward the output facet in the upward direction as shown in figure 6(a), is critical for increasing the slope efficiency. The light reflected by the DBR mirror interferes with the light radiated directly upward, so the resultant $\alpha_{\text{v\_up}}$ and η_{SE} are expected to change depending on the interference phase of the reflected and upward-radiated light. Although a DBR mirror has been employed in our previous device, the effect of this interference on the lasing characteristics was not investigated in detail, and η_{SE} of our previous device was no higher than 0.4–0.5 W A^{-1} [16].

To indicate the effect of reflection by the DBR mirror on η_{SE}, we rewrite equation (1) as follows:

$$\eta_{\text{SE}} = \frac{1.24}{\lambda}(1 - A)\eta_i \frac{\frac{1}{2}\left(1 + 2\sqrt{R}\cos\theta + R\right)\alpha_{\text{v}}}{\left(1 + \sqrt{R}\cos\theta\right)\alpha_{\text{v}} + \alpha_{\parallel} + \alpha_0}. \tag{2}$$

Here, R is the reflectivity of the DBR mirror and θ is interference phase between the reflected and upward-radiated light. For the above-designed photonic crystal structure, whose radiation constant $\alpha_{\text{v}} = 16$ cm^{-1}, we calculated upward radiation constant $\alpha_{\text{v\_up}}$, which is expressed by the term $\left[\frac{1}{2}\left(1 + 2\sqrt{R}\cos\theta + R\right)\alpha_{\text{v}}\right]$ in equation (2), and using equation (2) as functions of θ when $R = 0.9$; the results of these calculations are shown in figures 6(b) and (c). For comparison, values corresponding to an

Figure 7. (a) Top and (b) cross-sectional SEM images of photonic crystal fabricated for 500 μmΦ PCSEL. (c) Reflectivity of the fabricated DBR. Note that the SEM picture shown in (b) is flipped upside down, that is, the direction of epitaxial regrowth on the photonic crystal is depicted as downward. (d) *I–V* characteristics of the fabricated PCSELs with the DBR.

equivalent device without the DBR (i.e. when $R = 0.0$) are also shown with broken lines. When there is no DBR mirror, the downward radiation becomes loss, and, therefore, the slope efficiency is limited to $\sim$0.4 W A^{-1}. On the other hand, with the DBR mirror, a periodic dependence of $\alpha_{\mathrm{v\_up}}$ and η_{SE} on θ is observed. When interference is constructive (i.e. when θ is around 0°), $\eta_{\mathrm{SE}} \geqslant 0.8$ W A^{-1}, which is twice as high as that of our previous device, is obtained. We note that the term $\left[\left(1 + \sqrt{R}\cos\theta\right)\alpha_{\mathrm{v}} + \alpha_{\parallel} + \alpha_0\right]$ in equation (2) expresses the threshold gain for the lasing oscillation. Thus, the threshold current is also dependent on the interference phase θ.

3.4. Fabrication and lasing characteristics of the PCSELs

We fabricated a PCSEL based on the above-designed photonic crystal and DBR structures. Figure 7(a) shows a top-view SEM image of the fabricated photonic crystal after dry etching. The double-lattice structure, composed of circular and elliptical air holes, was successfully fabricated by an EB lithography and dry-etching process. We then performed MOVPE regrowth while retaining the air-hole structure inside the device, and formed the DBR mirror composed of 14 pairs of Al$_{0.1}$Ga$_{0.9}$As/Al$_{0.9}$Ga$_{0.1}$As layers (see figure 7(b)). For this DBR, R was measured to be $\sim$0.86 at the lasing wavelength of $\sim$940 nm as shown in figure 7(c). Figure 7(d) shows typical current–voltage (*I–V*) characteristics of the fabricated 500 μmΦ PCSELs with the DBR. Here, the interference phase varies with the thickness of the p-cladding layer, which determines the optical path length between the photonic crystal and the DBR mirror. In order to experimentally investigate the appropriate thickness of the p-cladding layer for realizing a high slope efficiency, we fabricated and evaluated the current–light output power (*I–L*) characteristics of four types of devices with p-cladding layer thicknesses of 1030 nm, 1080 nm, 1130 nm, and 1180 nm. Figures 8(a)–(d) show the *I–L* characteristics of each device, evaluated under pulsed conditions (with a repetition frequency of 1 kHz and a pulse width of 100 ns for a pulse duty cycle of 0.01%) at room temperature. The backside temperature of each device was kept at room temperature ($\sim$24 °C), because the device was driven under pulsed conditions with a low duty cycle, where the temperature rise was negligible. As shown in these figures, the slope efficiency and threshold current vary with the p-cladding layer thickness. The variations in slope efficiency and threshold current were checked by measuring three devices with the same p-cladding layer thickness, and were found to be very small. Figures 8(e) and (f) show the dependence of the slope efficiency and threshold current density on the p-cladding layer thickness, evaluated from these *I–L* characteristics. The slope efficiency and threshold current density are periodic over a change of $\sim$140 nm to the p-cladding layer thickness, corresponding to a change of one wavelength in the p-cladding layer. Constructive interference of the reflected and upward-radiated light is considered to occur at a p-cladding layer thickness of $\sim$1130 nm, resulting in a high slope efficiency exceeding 0.8 W A^{-1}. Comparison of these experimental results with the theoretical analysis in the section 3.3 allowed us to estimate the surface radiation constant and in-plane loss to be $\alpha_{\mathrm{v}} = 22$ cm^{-1} and $\alpha_{//} = 7$ cm^{-1}, assuming that α_0 and A are 6 cm^{-1} and 0.1, respectively. Fitting of the threshold current density was done assuming that the gain of the quantum wells, g, has a linear-fractional dependence [27] on
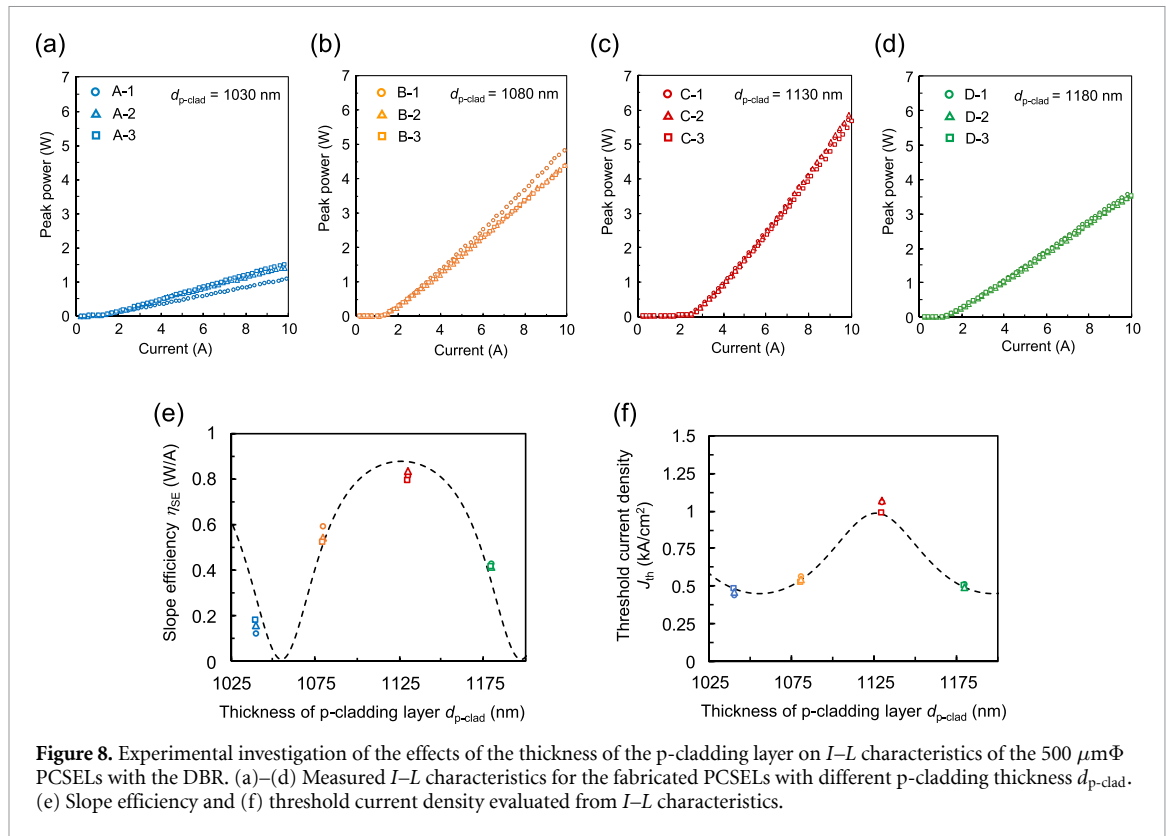
Figure 8. Experimental investigation of the effects of the thickness of the p-cladding layer on I–L characteristics of the 500 μmΦ PCSELs with the DBR. (a)–(d) Measured I–L characteristics for the fabricated PCSELs with different p-cladding thickness $d_{\text{p-clad}}$. (e) Slope efficiency and (f) threshold current density evaluated from I–L characteristics.

the carrier density, N, i.e. $g(N) = g_{\max}(N - N_{\text{tr}})/\{N + [g_{\max}/(-g_0)]N_{\text{tr}}\}$, where we set the transparency carrier density $N_{\text{tr}} = 1.5 \times 10^{18}$ cm^{-3}, the saturated gain $g_{\max} = 2000$ cm^{-1}, and the absorption coefficient in the absence of carriers $g_0 = -5000$ cm^{-1}.

Next, we evaluated the I–L characteristics and emitted beam patterns of a PCSEL, whose p-cladding layer thickness was set to 1130 nm, over a wider range of injected currents. Figure 9(a) shows the measured I–L characteristics. Owing to the high slope efficiency, a peak power exceeding 10 W was obtained at a lower current of $\sim$15 A than the previous device ($\sim$25 A) [16]. As shown in the measured far-field patterns of figure 9(b) and a single-spot beam with a narrow divergence angle of $\sim$0.1° (evaluated using the FWHM beam width) and $\sim$0.17° (evaluated using the 1/e^2 beam width) was achieved at an output power of 10 W. Such high-beam-quality operation clearly suggests that the laser operates in a single fundamental mode and that the oscillations of higher-order modes have been suppressed by virtue of the newly designed photonic crystal. We also attribute the narrow divergence angle ($\sim$0.1° at FWHM beam width) of the present device to the highly reflective DBR, which suppressed the direct nonuniform reflection effect from the p-side electrode. The nonuniform reflection from this electrode, which is only weakly reflective once it has been alloyed with the p$^+$-contact laser, is nevertheless considered to have been partly responsible for the wider divergence angle ($\sim$0.2° at FWHM beam width) in our previous device, which did not have a DBR.

Considering LiDAR applications, it is desirable for the PCSEL to operate over a wide temperature range. Accordingly, in addition to the characterization at room temperature as described above, we also evaluated the dependence of the lasing characteristics of the PCSEL on temperature. As mentioned in the introduction, the lasing spectrum of PCSELs has a small dependence on temperature. This is because the lasing spectrum is fixed by the lattice constant of the photonic crystal. The oscillation wavelength of the photonic crystal (and thus the emission wavelength of the PCSEL) changes by $\sim$0.08 nm °C^{-1} due to the change of the refractive index with temperature. However, it should be noted that the gain peak wavelength of the active layer (InGaAs/AlGaAs multiple quantum wells) also changes by $\sim$0.3 nm °C^{-1}, due to the change of its electronic bandgap with temperature. Due to these different rates of change, when the temperature is changed over a wide range, the deviation between the oscillation wavelength and the gain peak becomes large, which may cause an increase in the threshold current, a decrease in the output power, and mode hopping. Considering the above, for operation over a wide temperature range, we properly adjusted the lattice constant of the photonic crystal to minimize the deviation of the oscillation wavelength from the gain peak. To clarify the dependence of device performance on temperature, we evaluated the lasing characteristics under pulsed operation (with a repetition frequency of 1 kHz and a pulse width of 100 ns as above) at ambient temperatures ranging from -40 °C to 100 °C. Figure 10 shows the output power characteristics and lasing
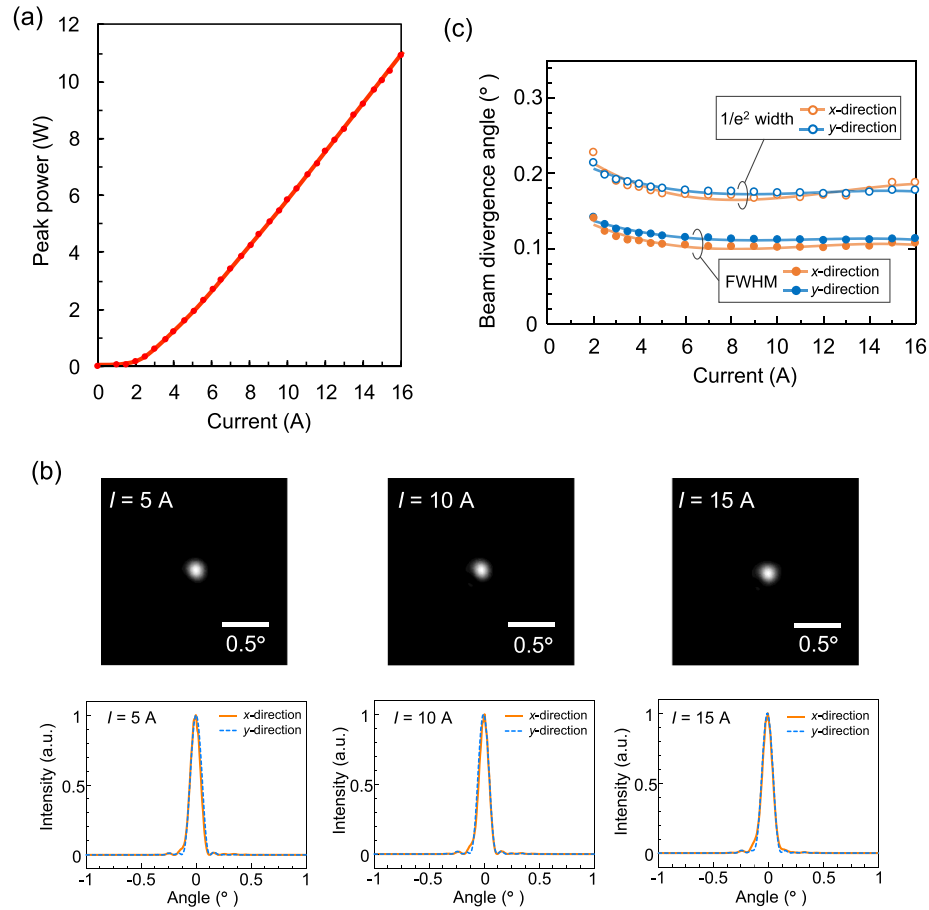
Figure 9. Measured lasing characteristics for a fabricated PCSEL with an optimized p-cladding layer thickness over a wide range of injected currents. (a) *I–L* characteristics, (b) far-field patterns, and (c) beam divergence angles evaluated using the FWHM and $1/e^2$ beam widths.
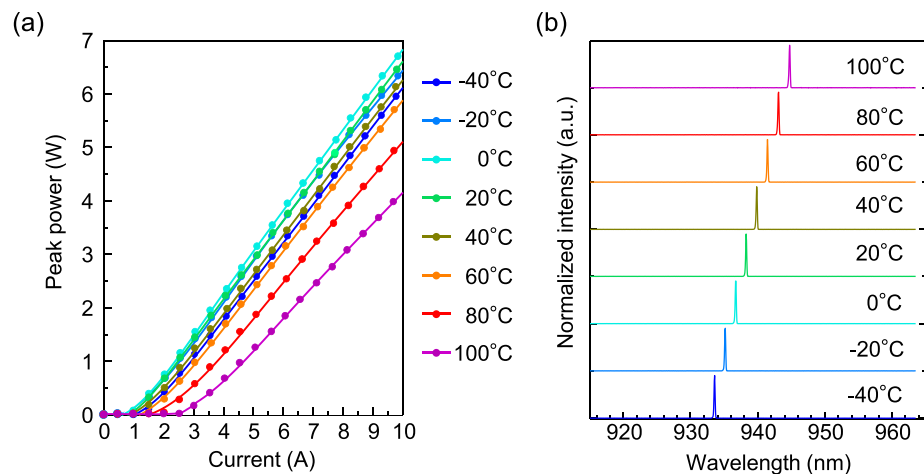
Figure 10. Temperature dependence (from −40 °C to 100 °C) of the lasing characteristics of the PCSEL. (a) *I–L* characteristics, (b) lasing spectra at various ambient temperatures. Lasing oscillation was obtained over the entire temperature range, and the average rate of change of output power with respect to temperature over this range was small, at ∼0.36% °C^{-1}, which is similar to that of commercially available FP-lasers (∼0.4% °C^{-1}). The temperature dependence of the lasing wavelength is maintained at ∼0.08 nm °C^{-1} in the range from −40 °C to 100 °C, which shows that the lasing wavelength is more stable than that of the conventional FP-lasers (∼0.30 nm °C^{-1}). It should be noted that the change in output power can be made smaller by further adjusting the lattice constant and the gain peak wavelength according to the required temperature range (for example, a range of high temperatures or low temperatures) for each application.
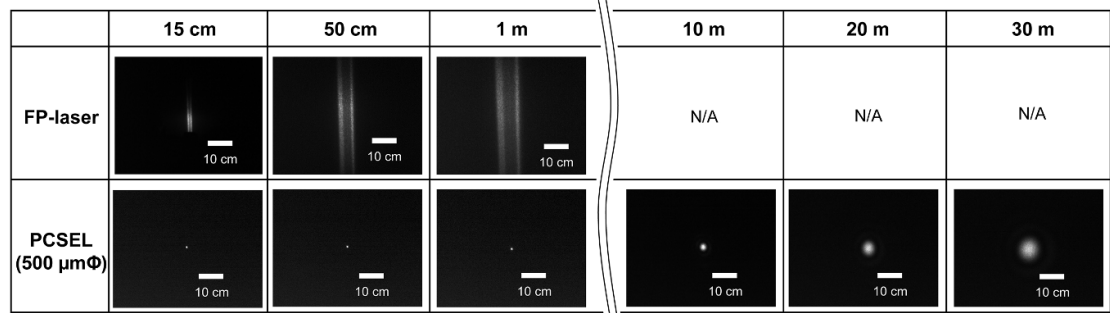
Figure 11. Beam propagation characteristics of the FP-laser and PCSEL without external lens.

spectrum at various temperatures. Lasing oscillation was obtained over the entire temperature range, and the average rate of change of output power with respect to temperature over this range was small, at $\sim$0.36% $^{\circ}$C^{-1}, which is similar to that of commercially available FP-lasers ($\sim$0.4% $^{\circ}$C^{-1}). It should be noted that the change in output power can be made smaller by further adjusting the lattice constant and the gain peak wavelength according to the required temperature range (for example, a range of high temperatures or low temperatures) for each application. In addition, figure 10(b) shows a narrow lasing spectrum at several temperatures, indicating that the laser operates in a stable lasing mode across the entire temperature range. The temperature dependence of the lasing wavelength is maintained at $\sim$0.08 nm $^{\circ}$C^{-1} in the range of -40 $^{\circ}$C to 100 $^{\circ}$C, which shows that the lasing wavelength is more stable than that of the conventional FP-lasers ($\sim$0.30 nm $^{\circ}$C^{-1}). These results clearly indicate that our PCSELs perform well under harsh practical conditions as required for LiDAR applications.
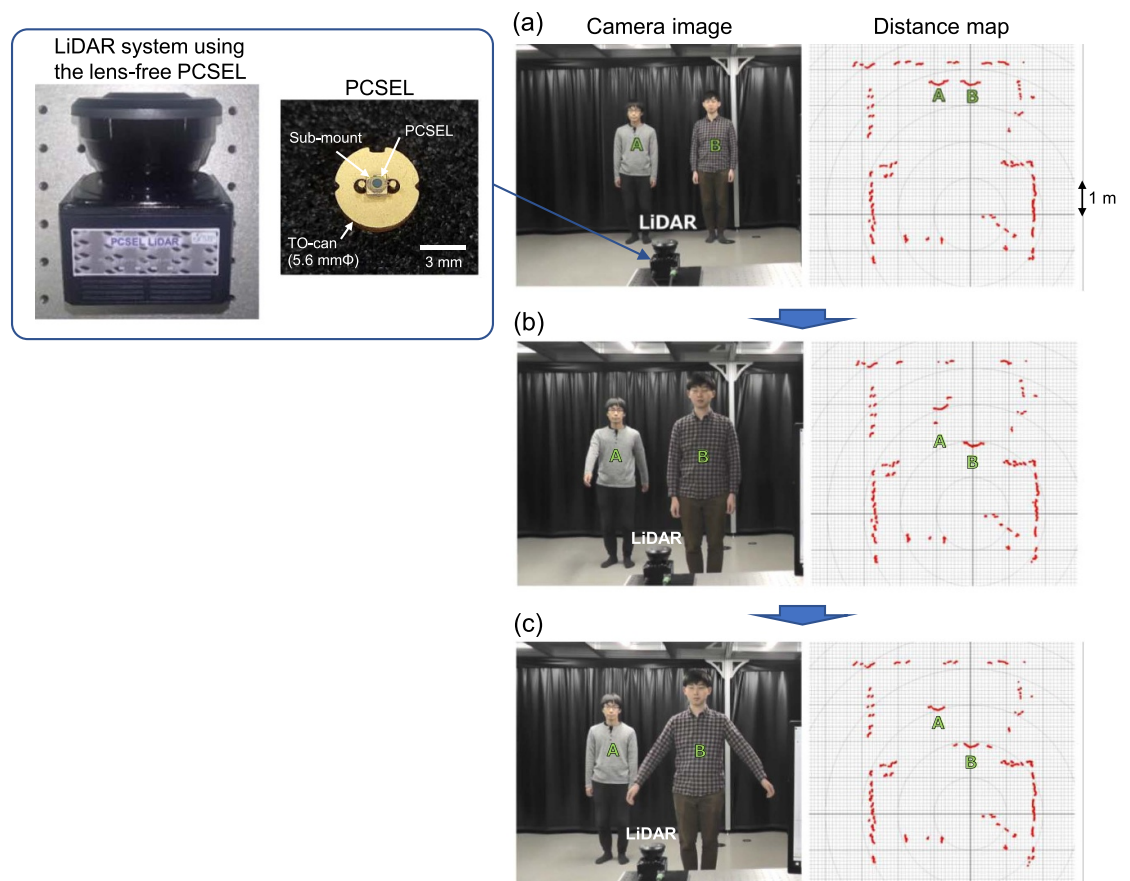
4. Demonstration of ToF LiDAR system using the lens-free PCSEL

High-power and narrow-beam-divergence operation of the PCSEL is advantageous for ToF LiDAR applications. Here, we use a lens-free PCSEL in a proof-of-concept demonstration of a compact, simplified ToF LiDAR system. First, we evaluate how small the beam diameter can be maintained when the emitted beam propagates in free space without the assistance of any external lens system. Figure 11 shows the beam pattern irradiated on a screen placed at distances from 15 cm to 30 m from the laser. For comparison, the results for a typical FP-laser are also shown. In the case of the FP-laser, the beam quickly spreads out because its divergence angles are large and asymmetric. Consequently, the beam pattern cannot be discerned after the beam has traveled beyond only 1 m. For this reason, a LiDAR system using typical FP-lasers requires an external, complicated lens system, which adds to the overall size and complexity of the LiDAR system. On the other hand, in the case of a PCSEL, whose beam divergence angles are much narrower than those of the FP-laser, the beam diameter is small even at distances far from the laser. Remarkably, a small circular beam of a diameter <5 cm (FWHM) is maintained even at a distance of 30 m. This result clearly suggests that an external lens system (and its associated complicated adjustment process) is not required for the PCSEL, allowing for the implementation of a much more compact, simplified LiDAR system.

Encouraged by the above results, we then developed a LiDAR system using the lens-free PCSEL. For comparison, we also prepared a LiDAR system using an FP-laser. Figure 12(a) shows a schematic diagram of the LiDAR system. As illustrated in the left panel of figure 12(a) and a beam was emitted from the light source and scanned in 1D using a rotating mirror, whereafter the light was collected by a detector (avalanche photodiode) [28]. The right panel of figure 12(a) shows the two types of light sources we used in this system: the first was the FP-laser used as a reference, which required a complex system of multiple lenses to correct the asymmetry of its beam, and the second was the PCSEL, which required no such lenses. We observed scanned beams projected on a screen (set at a distance of $\sim$1 m from each LiDAR system), where the beam was scanned at a pitch of 0.25° (figures 12(b) and (c)). For the system using the FP-laser, the large beam diameter caused the scanned beam patterns to overlap, so that the 0.25° pitch could not be resolved. However, for the system using the PCSEL, the scanned beam patterns did not overlap, and thus were clearly resolvable, owing to the narrow beam divergence angle of $\sim$0.1°. These results indicate that, by replacing the FP-laser with the PCSEL as the light source, not only can the external lens system be eliminated, but also can the spatial resolution and sensing performance of the overall LiDAR system be improved.
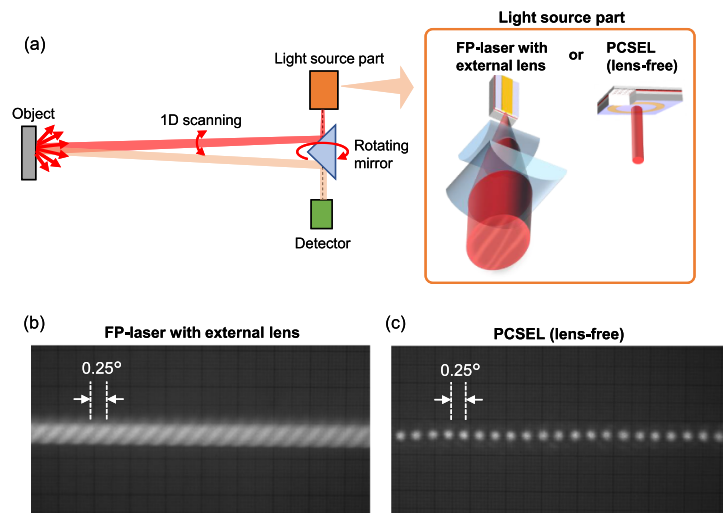
Figure 12. Comparison of LiDAR system using a conventional FP-laser with eternal lens and a lens-free PCSEL. (a) Schematic of our ToF LiDAR system. The light source consists of either an FP-laser with external lenses or a lens-free PCSEL. (b), (c) Beam patterns produced by scanning the beam at a pitch of 0.25° when the (b) FP-laser or (c) PCSEL is used as the light source. These lasers were driven at a peak current of 10 A, a pulse width of 2.5 ns, and the interval of the individual pulses of 18 μs. A rotational speed of mirror was set to 2300 rpm for a scan pitch of 0.25°.

Figure 13. Demonstration of real-time ToF sensing using the PCSEL-based LiDAR system. The insets show the LiDAR system and the PCSEL used for this system. (a)–(c) show real images and distance maps during the real-time ToF measurement.

We demonstrated real-time ToF sensing using the above PCSEL-based LiDAR system, as shown in figure 13 (and also in the supplementary video (available online at stacks.iop.org/JPPHOTON/3/022006/mmedia)). The developed LiDAR system and the PCSEL are shown in the inset of figure 13(a). Here, we sense two people (A, B) standing in front of the LiDAR system. The left panels are photographs and the right panels show the distances of the two people and their surroundings from the LiDAR system located at the

Figure 14. Various prospective applications of PCSELs for Society 5.0 [38].

intersection of the straight grey lines. First, persons A and B walk from distances of approximately 3.5 m to distances of approximately 3 m and 2 m, respectively (figures 13(a) and (b)). The distance map changes according to their movement, and the distance to each person is measured accurately throughout their motion. Next, person A moves his hands back and forth (figure 13(b)) and person B moves his hands left and right (figure 13(c)). The distance map clearly reflects the movement of these hands, owing to the high spatial resolution and accuracy of the LiDAR system. It was also confirmed that a maximum measuring distance of this system is ~20 m; this distance was limited by the LD driver current of ~10 A. This experiment serves as a successful demonstration of LiDAR using a lens-free PCSEL with sufficient functionality for autonomous robots and factory automation.

5. Summary and outlook

In this paper, we have first reviewed the progress and the state of the art of PCSEL technology, focusing on LiDAR applications which are attractive for smart mobility. The unique features of a PCSEL that are desirable for LiDAR applications, including its high-power, very-narrow-divergence, and symmetric beam, narrow linewidth, and small spectral temperature dependence, are owed to its broad-area, coherent band-edge resonance. Following the summary of current progress of PCSELs, we have described the concept of double-lattice photonic crystals that we have recently proposed as a key for high-power, high-beam-quality (narrow-beam-divergence) operation of broad-area ($\geqslant$500 μmΦ) PCSELs. Next, we have designed a photonic crystal structure suitable for a PCSEL with a 500 μmΦ resonator. Also, we have optimized the reflection phase of a backside DBR mirror to improve the slope efficiency of a single laser device to ~0.8 W A^{-1}, which is twice as high as our previously reported PCSELs. With our new PCSEL, we have demonstrated pulsed operation with a high peak power of 10 W and a nearly diffraction-limited beam divergence angle of ~0.1° at FWHM under room-temperature, pulsed operation. In addition, we have evaluated the lasing characteristics at ambient temperatures ranging from -40 °C to 100 °C. The laser operates in a stable lasing mode across the entire temperature range, and the rates of change of output power and lasing wavelength with respect to temperature over this range were small, at ~0.36% °C^{-1} and ~0.08 nm °C^{-1}, respectively. These results clearly indicate that our PCSELs perform well under harsh practical conditions as required for LiDAR applications.

Then, we have implemented this PCSEL in a ToF LiDAR system and have demonstrated real-time ToF sensing. In contrast to existing systems using typical FP-lasers, our PCSEL-based LiDAR system required no external lens system at its light source, owing to the narrow beam divergence of the PCSEL. The elimination of the requirement for such lenses will lead to the miniaturization and simplification of LiDAR systems. We also have shown that the narrow beam divergence of the PCSEL-based LiDAR led to an improvement of the overall spatial resolution of the system.

Our demonstration clearly evinces the suitability of photonic crystal lasers as light sources for compact, affordable, and reliable LiDAR systems. PCSEL will also be applied to sensing at longer distance ($\sim$100 m) for autonomous vehicles in the future, since the output power increases and the beam divergence angle decreases in proportion to the coherent lasing area. The issue of eye safety at such high power operation can be resolved by reducing the pulse width to a few tens of picoseconds by introducing into these PCSELs a Q-switching mechanism [29], or by constructing double-lattice PCSELs with a longer lasing wavelength of 1.3 μm [5, 30]. In addition, owing to their small beam size, these PCSELs may find use in combination with mechanical or non-mechanical beam-scanning devices currently under intensive research elsewhere [31–33], such as microelectromechanical systems (MEMS) scanning mirrors [34, 35]. Furthermore, very recently, we have succeeded in realizing a non-mechanical, electrical 2D beam-scanning laser chip with high, watt-class output power and a high beam quality by introducing the concept of 'dually modulated' photonic crystals [36], which will allow for the omission of not only the external lens but also the mechanical beam scanner in the future. We believe that PCSELs will be ideal light sources for simple, compact, affordable, and reliable next-generation LiDAR systems, and that their capability of high-power, high-beam-quality operation (under both pulsed and continuous-wave conditions [16, 37]) and their many unique functionalities will also unlock a wider range of applications in fields such as material processing, adaptive lighting, projection, and the life sciences (see figure 14).

Acknowledgments

ORCID iDs

Masahiro Yoshida ● https://orcid.org/0000-0003-0653-8189
Menaka De Zoysa ● https://orcid.org/0000-0002-1246-2750
Kenji Ishizaki ● https://orcid.org/0000-0001-7199-8523
Takuya Inoue ● https://orcid.org/0000-0002-8206-8206
Susumu Noda ● https://orcid.org/0000-0003-4302-0549

References

[1] Lalonde J F, Vandapel N, Huber D and Hbert M 2006 *J. Field Robot.* **23** 839
[2] Weiss U and Biber P 2011 *Robot. Auton. Syst.* **59** 265
[3] Luettel T, Himmelsbach M and Wuensche H J 2012 *Proc. IEEE* **100** 1831
[4] Puente I, Gonzalez-Jorge H, Martinez-Sanchez J and Arias P 2013 *Measurment* **46** 2127
[5] Imada M, Noda S, Chutinan A and Tokuda T 1999 *Appl. Phys. Lett.* **75** 316
[6] Riechel S, Kallinger C, Lemmer U and Feldmann J 2000 *Appl. Phys. Lett.* **77** 2310
[7] Noda S, Yokoyama M, Imada M, Chutinan A and Mochizuki M 2001 *Science* **293** 1123
[8] Imada M, Chutinan A, Noda S and Mochizuki M 2002 *Phys. Rev.* B **65** 195306
[9] Ryu H Y, Kwon S H, Lee Y J, Lee Y H and Kim J S 2002 *Appl. Phys. Lett.* **80** 3476
[10] Miyai E, Sakai K, Okano T, Kunishi W, Ohnishi D and Noda S 2006 *Nature* **441** 946
[11] Kim M, Kim C S, Bewley W W, Lindle J R, Canedy C L, Vurgaftman I and Meyer J R 2006 *Appl. Phys. Lett.* **88** 191105
[12] Matsubara H, Yoshimoto S, Saito H, Jianglin Y, Tanaka Y and Noda S 2008 *Science* **319** 445
[13] Kurosaka Y, Iwahashi S, Liang Y, Sakai K, Miyai E, Kunishi W, Ohnishi D and Noda S 2010 *Nat. Photon.* **4** 447
[14] Hirose K, Liang Y, Kurosaka Y, Watanabe A, Sugiyama T and Noda S 2014 *Nat. Photon.* **8** 406
[15] Noda S, Kitamura K, Okino T, Yasuda D and Tanaka Y 2017 *IEEE J. Sel. Top. Quantum Electron.* **23** 4900107
[16] Yoshida M, De Zoysa M, Ishizaki K, Tanaka Y, Kawasaki M, Hatsuda R, Song B S, Gelleta J and Noda S 2019 *Nat. Mater.* **18** 121
[17] Meier M, Mekis A, Dodabalapur A, Timko A, Slusher R E, Joannopoulos J D and Nalamasu O 1999 *Appl. Phys. Lett.* **74** 7
[18] Iwahashi S, Kurosaka Y, Sakai K, Kitamura K, Takayama N and Noda S 2011 *Opt. Express* **19** 11963
[19] Kitamura K, Nishimoto M, Sakai K and Noda S 2012 *Appl. Phys. Lett.* **101** 221103
[20] Sakai K, Miyai E and Noda S 2006 *Appl. Phys. Lett.* **89** 021101
[21] Sakai K, Miyai E and Noda S 2010 *IEEE J. Quantum Electron.* **46** 788
[22] Liang Y, Peng C, Sakai K, Iwahashi S and Noda S 2011 *Phys. Rev.* B **84** 195119
[23] Yoshida M, Kawasaki M, De Zoysa M, Ishizaki K, Hatsuda R and Noda S 2016 *Appl. Phys. Express* **9** 062702
[24] De Zoysa M, Yoshida M, Kawasaki M, Ishizaki K, Hatsuda R, Tanaka Y and Noda S 2017 *IEEE Photonics Technol. Lett.* **29** 1739
[25] Hamamatsu Photonics Photonic crystal surface emitting laser diodes (PCSEL) (available at: www.hamamatsu.com/jp/en/product/lasers/semiconductor-lasers/pcsels/index.html)
[26] Yoshida M, Kawasaki M, De Zoysa M, Ishizaki K, Inoue T, Tanaka Y, Hatsuda R and Noda S 2020 *Proc. IEEE* **108** 819
[27] Chen S, Yoshita M, Ito T, Mochizuki T, Akiyama H and Yokoyama H 2013 *Opt. Express* **21** 7570

[28] Inoue K 2017 *The 145th Microoptics Meeting Fresh Topics in Smart Sensing and Smart Imaging*

[29] Morita R, Inoue T, De Zoysa M, Ishizaki K and Noda S 2021 *Nat. Photon.* (https://doi.org/10.1038/s41566-021-00771-5)

[30] Itoh Y *et al* 2020 *Opt. Express* **28** 35483

[31] Lindle J R, Watnik A T and Cassella V A 2016 *Appl. Opt.* **55** 4336

[32] Zohrabi M, Lim W Y, Cormack R H, Supekar O D, Bright V M and Gopinath J T 2019 *Opt. Express* **27** 4404

[33] Wang Y, Zhou G, Zhang X, Kwon K, Blanche P A, Triesault N, Yu K S and Wu M C 2019 *Optica* **6** 557

[34] Holmstrom S T S, Baran U and Urey H 2014 *J. Microelectromech. Syst.* **23** 259

[35] Yoo H W, Cruml N, Brunner D, Schwarzl C, Thurner T, Hennecke M and Schitter G 2018 *Elektrotech. Inftech.* **135** 408

[36] Sakata R *et al* 2020 *Nat. Commun.* **11** 3487

[37] De Zoysa M *et al* 2020 *J. Opt. Soc. Am.* B **37** 3882

[38] Government of Japan Society 5.0 proposed by the Japanese government as a future society (available at: www8.cao.go.jp/cstp/english/society5_0/index.html)